arXiv:astro-ph/0501267v1 13 Jan 2005

Preprint no. NSF-KITP-04-127; submitted to ApJ July 22, 2004; accepted January 5, 2005

Three-Dimensional Vortices in Stratified Protoplanetary Disks

Joseph A. Barranco[1]

Kavli Institute for Theoretical Physics, Kohn Hall, University of California, Santa Barbara, CA 93106

barranco@kitp.ucsb.edu

and

Philip S. Marcus

Department of Mechanical Engineering, Etcheverry Hall, University of California, Berkeley, CA 94720

pmarcus@kepler.berkeley.edu

ABSTRACT

We present the results of high-resolution, three-dimensional (3D) hydrodynamic simulations of the dynamics and formation of coherent, long-lived vortices in stably-stratified protoplanetary disks. Tall, columnar vortices that extend vertically through many scale heights in the disk are unstable to small perturbations; such vortices cannot maintain vertical alignment over more than a couple scale heights and are ripped apart by the Keplerian shear. Short, finite-height vortices that extend only one scale height above and below the midplane are also unstable, but for a different reason: we have isolated an antisymmetric (with respect to the midplane) eigenmode that grows with an e-folding time of only a few orbital periods; the nonlinear evolution of this instability leads to the destruction of the vortex. Serendipitously, we observe the formation of 3D vortices that are centered not in the midplane, but at one to three scale heights above and below. Breaking internal gravity waves create vorticity; anticyclonic regions of vorticity roll-up and coalesce into new vortices, whereas cyclonic regions shear into thin azimuthal bands. Unlike the midplane-centered vortices that were placed *ad hoc*

[1]NSF Astronomy & Astrophysics Postdoctoral Fellow

in the disk and turned out to be linearly unstable, the off-midplane vortices form naturally out of perturbations in the disk, and are stable and robust for many hundreds of orbits.

Subject headings: accretion, accretion disks — hydrodynamics — planetary systems: protoplanetary disks

1. INTRODUCTION

Like the atmosphere of Jupiter, protoplanetary disks are characterized by rapid rotation and intense shear, inspiring proposals that disks may also be populated with long-lived, robust storms analogous to the Great Red Spot (Barge & Sommeria 1995; Adams & Watkins 1995). Such vortices may play key roles in the formation of stars and planets: (1) in cool, neutral protoplanetary disks, vortices might transport angular momentum radially outward so that mass can continue to accrete onto the growing protostar; (2) models of protoplanet migration (that account for "Hot Jupiters," gas giant planets that closely orbit their parent stars with periods of only a few days) are highly sensitive to the effective "viscosity" or turbulent transport within disks; transport mediated by coherent vortices rather than turbulent eddies could lead to qualitative and quantitative changes to migration rates; and (3) vortices rapidly sweep-up and concentrate dust particles, which may help in the formation of kilometer-size planetesimals, the "building blocks" of planets, either by increasing the efficiency of binary agglomeration or by triggering a local gravitational instability.

1.1. The angular momentum problem in accretion disks

One of the most vexing problems in astrophysics is how mass and angular momentum are transported in accretion disks. Because disks are differentially rotating, one might think that viscous torquing could transport angular momentum outward and mass inward onto the central object. However, if the source of viscosity is molecular collisions, then the time-scale for such viscous transport would exceed the age of the universe by many orders of magnitude. Shakura & Sunyaev (1973) proposed that turbulence might enhance the transport, and so introduced a turbulent or "eddy" viscosity: $\nu_t = \alpha H c_s$, where H is the pressure scale height of the disk, c_s is the sound speed, and α is a dimensionless number (less than unity because turbulent eddies would most likely be subsonic and no larger than the scale height of the disk). The source of this turbulence (e.g., shear instabilities, convection, finite-amplitude perturbations, magnetic fields), to say the least, has been highly controversial. See Balbus

& Hawley (1998) and Stone et al. (2000) for thorough reviews.

Balbus & Hawley (1991) (also Hawley & Balbus 1991) applied the magneto-rotational instability (MRI) of Velikhov (1959) and Chandrasekhar (1960, 1961), and demonstrated that weak magnetic fields can destabilize the Keplerian shear in an accretion disk, leading to the creation of turbulence and the outward transport of angular momentum. However, the relatively cool and nearly neutral accretion disks around protostars most likely lack sufficient coupling between matter and magnetic fields (Blaes & Balbus 1994), except perhaps in thin surface layers that have been ionized by cosmic rays or protostellar x-rays (Gammie 1996).

Thus, there still remains strong interest in finding a purely hydrodynamic means of mass and angular momentum transport. Bracco et al. (1998), using two-dimensional, incompressible fluid dynamics, have shown that long-lived, coherent anticyclonic vortices emerge out of a Keplerian shear flow that is seeded with small-scale vorticity perturbations; they observed smaller vortices merging to form larger vortices, demonstrating the "inverse cascade" of energy from small to large scales that is a hallmark of two-dimensional turbulent flows (Provenzale 1999). Godon & Livio (1999, 2000) confirmed this result with two-dimensional, compressible, barotropic simulations. Lovelace et al. (1999) have found a linear instability of nonaxisymmetric Rossby waves in thin, non-magnetized Keplerian disks when there is a local extremum in an entropy-modified potential vorticity. Li et al. (2000, 2001) showed that such Rossby waves break and coalesce to form vortices which radially migrate and transport mass through the disk. Klahr & Bodenheimer (2003) have demonstrated that a globally unstable radial entropy gradient in a protoplanetary disk generates Rossby waves, vortices and turbulence that may result in local outward transport of angular momentum. To date, there are still unresolved issues regarding realistic formation mechanisms and long-term maintenance of vortices in disks.

1.2. The role of turbulence and vortices in planet formation

Whether protoplanetary disks are filled with turbulent eddies or long-lived coherent vortices (or both) is critical for not only accretion, but also for two key processes in planet formation: protoplanet migration and planetesimal formation. Extrasolar planet surveys reveal a class of gas giant planets that closely orbit their parent stars with periods of only a few days (Mayor & Queloz 1995; Marcy & Butler 1998; Marcy et al. 2000). These "Hot Jupiters" most likely did not form *in situ*, but instead formed farther out in their disks where it was cooler, and then migrated inward to their present locations (Lin et al. 1996). The exact mechanism for this migration depends on the size of the protoplanet: a small protoplanet ($\lesssim 10 M_\oplus$) raises tides in the disk which exert torques back on the protoplanet, causing it to

migrate inward (Type I migration), whereas a larger protoplanet opens up a gap in the disk, and both gap and protoplanet migrate inward together on a slow "viscous" timescale (Type II migration) (Ward 1997). In numerical simulations of protoplanet migration, the viscous evolution is usually modeled with an eddy viscosity. Although such a crude turbulence model is useful for estimating global disk properties, it is not at all clear that it is appropriate to apply it to complex disk-planet interactions. Does a turbulent disk really behave exactly the same way as a laminar disk with just a larger viscosity? Qualitatively and quantitatively, transport and mixing due to long-lived coherent vortices are not necessarily well modeled by an enhanced viscosity (Koller et al. 2003).

Another aspect of planet formation that is extremely sensitive to turbulence is the formation of planetesimals, the kilometer-size "building blocks" of planets. In a quiescent, laminar protoplanetary disk, planetesimals may form directly from the gravitational clumping of a thin, dense dust sublayer that has settled into the midplane (Safranov 1960; Goldreich & Ward 1973). However, turbulence (either from MRI, or generated by Kelvin-Helmholtz-like instabilities of the vertical shear between the dust sub-layer in the midplane, which orbits at the Keplerian velocity, and the gas-rich layers immediately above and below it, which orbit at a slightly slower rate because of the outward gas pressure force) might "kick up" the dust and prevent the sub-layer from reaching the critical density necessary for gravitational instability (Cuzzi et al. 1993; Weidenschilling 1995; Champney et al. 1995). Further growth of grains must instead continue via binary agglomeration (Weidenschilling & Cuzzi 1993).

Vortices may aid in the formation of planetesimals in either scenario. Barge & Sommeria (1995), Tanga et al. (1996), Chavanis (2000), and de la Fuente Marcos & Barge (2001) tracked the motion of individual particles in analytic models of two-dimensional anticyclones embedded in Keplerian shear. Klahr & Henning (1997) considered simple models of vortices that corresponded to convective cells. Johansen et al. (2004) used two-fluid simulations to study the interactions of the gas and dust components inside vortices. However, because of the relatively low resolution and high numerical dissipation in their simulations, their vortices were short-lived and decayed away in roughly one orbit. In all these models, gas drag caused grains to spiral into the vortex centers. Density enhancements inside vortices might increase the efficiency of binary agglomeration, or might trigger *local* gravitational clumping within the vortex center as opposed to the global gravitational clumping of the whole dust sub-layer envisioned in the original Safranov (1960) and Goldreich & Ward (1973) theory.

1.3. Outline

This work is the first in a series on high-resolution numerical simulations of the dynamics and formation of long-lived, coherent vortices in protoplanetary disks, and on what role they may play in star and planet formation. In §2, we will overview dimensional analysis and key timescales for vortices in protoplanetary disks. We will discuss the deficiencies of 2D analyses and explain the need for 3D simulations. In §3, we will present the hydrodynamical equations for the base disk and the vortex flow, as well as briefly describe the numerical method. Results of numerical simulations will be presented in §4, including a discussion on angular momentum transport. Conclusions and avenues for future work appear in §5.

2. A PRIMER FOR VORTEX DYNAMICS IN DISKS

2.1. Dimensional analysis and key timescales

Protoplanetary disks are cool in the sense that the gas sound speed c_s is much slower than the Keplerian orbital velocity $V_K(r) \equiv r\Omega_K(r) \equiv \sqrt{GM_\star/r}$, where G is the gravitational constant, $M_\star$ is the protostellar mass, and r is the cylindrical radius to the protostar. Hydrostatic balance implies that the time it takes sound waves to traverse the thickness of the disk is of order the orbital period. Thus, cool disks are geometrically thin (see Frank et al. 1985):

$$c_s \sim \Omega_K H, \tag{2-1a}$$

$$\delta \equiv c_s/V_K \sim H/r < 1, \tag{2-1b}$$

where H is the vertical pressure scale height. The radial component of the protostellar gravity nearly balances the centrifugal force, but because of the relatively weak outward radial pressure force, the gas orbits at slightly slower than the Keplerian velocity:

$$\Omega(r,z) = \Omega_K(r)\left[1 - \eta(r,z)\right], \tag{2-2}$$

where $\eta \sim \mathcal{O}(\delta^2)$. The horizontal shear rate of this base flow is:

$$\sigma_K \equiv r\frac{\partial \Omega_K}{\partial r} = -\frac{3}{2}\Omega_K. \tag{2-3}$$

Keplerian shear is anticyclonic (as indicated by the negative sign), and is comparable in magnitude to the rotation rate itself. As we will see, this has important consequences for the properties of vortices in protoplanetary disks.

Shear will stretch and tear a vortex apart unless: (1) the vortex rotates in the same sense as the ambient shear, and (2) the vortex is at least as strong as the shear (Moore & Saffman 1971; Kida 1981; Marcus 1990, 1993). The first condition implies that all long-lived vortices in a protoplanetary disk will be anticyclones; that is, the vortices will rotate in a sense opposite of that of the overall rotation of the disk. Let $\tilde{v}_\perp$ be the characteristic horizontal speed of gas around a vortex with aspect ratio $\chi \equiv \Lambda_\phi/\Lambda_r > 1$, where Λ_r (along the radial direction in the disk) is the minor axis and Λ_ϕ (along the azimuthal direction in the disk) is the major axis. The characteristic z-component of vorticity[1] in the core of the vortex is $\tilde{\omega}_z \sim \tilde{v}_\perp/\Lambda_r$. The second condition above implies that the horizontal speed of gas around the vortex must be of order the differential velocity across the vortex due to the ambient shear, or equivalently, that the characteristic vorticity is of order the shear rate: $\tilde{\omega}_z \sim \tilde{v}_\perp/\Lambda_r \sim \sigma_K$. Moore & Saffman (1971) and Kida (1981) analytically determined the exact steady-state solution for a 2D elliptical vortex of uniform vorticity embedded in a uniform shear and showed that:

$$\frac{\tilde{\omega}_z}{\sigma} = \left(\frac{\chi+1}{\chi-1}\right)\frac{1}{\chi}, \tag{2-4}$$

for a vortex that rotates in the same sense as the shear. A vortex that is weak relative to the shear will be stretched out and have a large aspect ratio, whereas a vortex that is comparable in strength to the shear will be more compact and have an aspect ratio closer to unity. Because the Keplerian shear is comparable in magnitude to the Keplerian rotation rate, the rotational period of gas around the core of the vortex, $\tau_{vor} \equiv 4\pi/\tilde{\omega}_z$, is of order the orbital period of the vortex around the protostar, $\tau_{orb} \equiv 2\pi/\Omega$. The Rossby number is defined to be the ratio of these two timescales:

$$Ro \equiv \frac{\tilde{\omega}_z}{2\Omega} \sim \frac{\tau_{orb}}{\tau_{vor}} \sim \frac{3}{4}\frac{\chi+1}{\chi-1}\frac{1}{\chi}, \tag{2-5}$$

which is order unity for compact vortices. In contrast, the Great Red Spot (GRS) on Jupiter rotates with a period of roughly six days, whereas the planet rotates in just under 10 hours, implying a Rossby number $Ro \approx 0.18$ (Marcus 1993).[2]

As we are interested in long-lived vortices, we require that the gas velocity be subsonic; otherwise, sound waves and shocks would rapidly dissipate the kinetic energy of the vortex. Equations (2-1a) and (2-5) imply:

$$\epsilon \equiv \frac{\tilde{v}_\perp}{c_s} \sim \frac{\Lambda_r}{H} Ro, \tag{2-6}$$

---

[1]Recall that vorticity is defined $\omega \equiv \nabla \times \mathbf{v}$, and is *two times* the local angular velocity of the fluid.

[2]For a rotating planet, $Ro \sim (\tau_{orb}/\sin\lambda)/\tau_{vor}$, where λ is the latitude. Only the component of the rotation normal to the surface of the planet enters into the horizontal component of the Coriolis force.

where ϵ is defined to be the horizontal Mach number. *Thus, the horizontal extent of subsonic, compact vortices in a Keplerian shear cannot be much greater than the scale height of the disk.* Such vortices are 3D in nature. In contrast, the GRS has considerably more "pancake-like" dimensions: 26,000 km × 13,000 km × 40 km (Marcus 1993).

Another important timescale is the Brunt-Väisälä period: $\tau_{BV} \equiv 2\pi/\omega_{BV}$, which is the period of oscillations in a convectively stable atmosphere (e.g., internal gravity waves). The Brunt-Väisälä frequency is (see Pedlosky 1979): $\omega_{BV} \equiv \sqrt{(g/C_p)\partial\bar{s}/\partial z}$, where g is the local gravitational acceleration, C_p is the specific heat at constant pressure, and $\bar{s}$ is the mean entropy. If the protoplanetary disk is vertically isothermal, then $\omega_{BV} \approx \Omega_K|z|/H$. That is, except in the immediate vicinity of the midplane, the Brunt-Väisälä period is also of order the orbital period in the disk. The internal Froude number is defined as the ratio of the Brunt-Väisälä period to the rotational period of the gas in a vortex:

$$Fr \equiv \frac{\tilde{\omega}_z}{2\omega_{BV}} \sim \frac{\tau_{BV}}{\tau_{vor}} \sim \left(\frac{H}{z}\right) Ro. \tag{2-7}$$

When the Froude number is much less than unity, a system is considered to be strongly stratified; large-scale vertical motions are suppressed and the different layers of the fluid are only weakly coupled.

Table 1 summarizes the values of the key timescales discussed so far. For comparison, values for the GRS are presented as well. On Jupiter, these timescales are well ordered: $\tau_{vor} \gg \tau_{orb} \gg \tau_{BV}$; whereas in a protoplanetary disk: $\tau_{vor} \sim \tau_{orb} \sim \tau_{BV}$. The near-equality of timescales in a protoplanetary disk simply follows from the fact that at any given location in the disk, the protostellar gravity sets the orbital velocity, shear, and strength of the stratification. Because the Brunt-Väisälä frequency for the GRS is so much faster than the other timescales, the vertical and horizontal dynamics can be decoupled; the GRS is well-modeled with two-dimensional fluid dynamics. No such clear separation of timescales occurs for a protoplanetary disk, and the horizontal and vertical dynamics cannot be decoupled. In general, when the Rossby and Froude numbers are small (e.g., rotation and stratification dominate over shear and nonlinear advection), then the horizontal and vertical motions can usually be decoupled and two-dimensional analyses can safely be applied.

In many of the common 2D models (e.g., "shallow-water", quasigeostrophic, or 2D-barotropic), vorticity (or a potential vorticity) is an advectively conserved quantity (because baroclinicity and vortex tilting are neglected). In 2D, only the z-component of vorticity is nonzero, and vortex lines can only be oriented vertically. The rotation axes of long-lived coherent vortices as well as transient turbulent eddies are constrained to be aligned parallel (or anti-parallel) to the vertical axis. Furthermore, shear will stretch out and destroy those vortices that do not have the same sense of rotation as the shear. Thus, a 2D shear flow

will be populated with vortices that are all perfectly aligned vertically and with the same sense of rotation. It has been demonstrated in both laboratory experiments and numerical simulations that in such restricted flows, small regions of vorticity merge to form larger vortices — this phenomenon is called an "inverse cascade" of energy from small to large scales (Kraichnan 1967; Lesieur 1997; Paret & Tabeling 1998; Baroud et al. 2003) Out of an apparently chaotic flow filled with small-scale, transient eddies, large-scale coherent features can emerge.

In 3D, the dynamics of turbulence are very different. Vortex lines can be oriented in any direction, and they can twist and bend. Vortices and eddies tilt and stretch their neighbors, disrupting them and eventually destroying them as they give up their energy to smaller eddies. In fact, this is the foundation for the Richardson and Kolmogorov model of 3D, isotropic turbulence: turbulent kinetic energy is transfered (via nonlinear interactions) from large to small to smaller eddies on down (i.e., "forward cascade") until it is destroyed by viscous dissipation.

An open question (and a very active area of basic research in fluid dynamics) is what happens when rotation and stratification are important, but not overwhelmingly dominant (e.g., when the Rossby and/or Froude numbers are of order unity)? How much rotation and stratification are necessary for a real, 3D flow to exhibit 2D characteristics, such as inverse cascades? Bracco et al. (1998) and Godon & Livio (1999, 2000) showed that small vortices merged to form larger vortices in 2D simulations, but these results have yet to be confirmed with 3D simulations.

2.2. A model of a 3D vortex

One of the best ways to visualize a vortex in three dimensions is to graph vortex lines, curves that are everywhere tangent to the vorticity vector field. Vorticity is, by definition, divergence-free; thus, vortex lines (like magnetic field lines) cannot have beginnings or endings within the fluid, but must extend to the boundaries, or off to infinity, or form closed loops. The simplest example of a 3D vortex is an infinite column of rotating fluid in which the fluid velocity is independent of height. The core of uniform vorticity is threaded by infinitely-long parallel vortex lines (see Figure 1a). One might imagine chopping off the ends of an infinite column to create a finite-height cylinder of rotating fluid. However, vortex lines cannot have loose ends in the fluid, and instead must wrap-around and form closed loops (see Figure 1b). Note that in the core of such a vortex, the vortex lines will be oriented in one direction, whereas in a halo surrounding the core, the vortex lines will be oriented in the opposite direction.

Timescale	GRS	PPD
$\tau_{vor} \equiv 4\pi/\tilde{\omega}_z$	8 d.	~ 1 y.
$\tau_{orb} \equiv 2\pi/\Omega$	10 h.	~ 1 y.
$\tau_{BV} \equiv 2\pi/\omega_{BV}$	6 m.	~ 1 y.
$Ro \equiv \tau_{orb}/\tau_{vor}$	0.18	$\mathcal{O}(1)$
$Fr \equiv \tau_{BV}/\tau_{vor}$	5×10^{-4}	$\mathcal{O}(1)$
$Ri \equiv 1/Fr^2$	4×10^6	$\mathcal{O}(1)$

Table 1: Comparison of important dynamical timescales for the Great Red Spot and a vortex in a protoplanetary disk. Here, we use "year" in the more general sense to refer to the orbital period in the disk. τ_{vor} is the orbital period of gas around the core of the vortex, τ_{orb} is the rotational period of the system, and τ_{BV} is the Brunt-Väisälä period, or the timescale for vertical thermal oscillations in a stably stratified atmosphere. Note that for the GRS, $\tau_{vor} \gg \tau_{orb} \gg \tau_{BV}$, whereas for the PPD, $\tau_{vor} \approx \tau_{orb} \approx \tau_{BV}$. The lower half of the table expresses the same data in terms of common nondimensional parameters from fluid dynamics: the Rossby number, the internal Froude number, and the Richardson number. For a planetary atmosphere, only the component of the rotation vector normal to the surface is relevant, so the Rossby number is larger by a factor $1/\sin\lambda$, where λ is the latitude on the planet.

Variable	Scaling
$\tilde{v}_\perp/c_s$	$\epsilon \sim (\Lambda_r/H)Ro$
$\tilde{p}/\bar{p} \sim \tilde{\rho}/\bar{\rho} \sim \tilde{T}/\bar{T}$	ϵ^2/Ro
$\tilde{v}_z/c_s$	$< \epsilon^2$

Table 2: How velocity and thermodynamic variables scale with Mach number ϵ and Rossby number Ro.

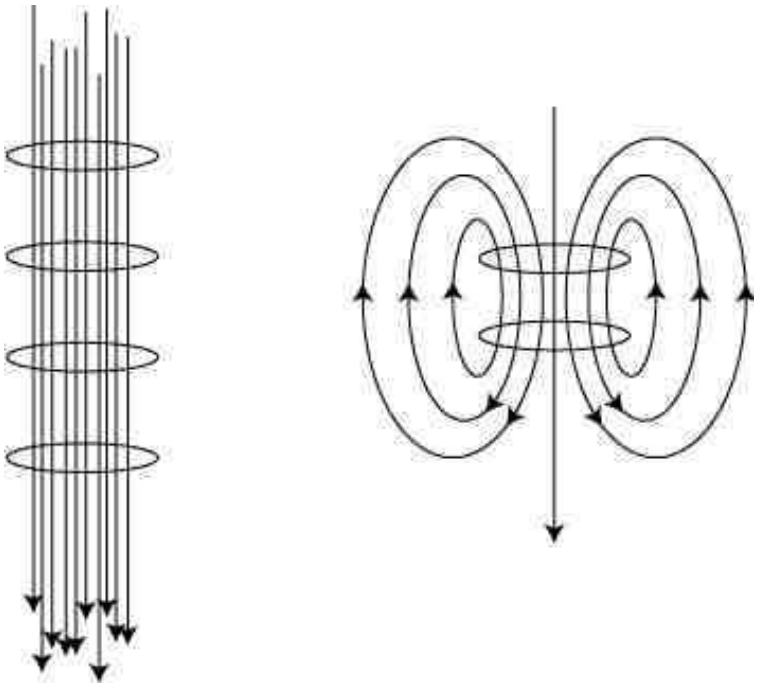

Fig. 1.— Vortex lines in an infinite columnar vortex and a finite-height cylindrical vortex. Downward oriented arrows denote anticyclonic vorticity, whereas upward-oriented arrows indicate cyclonic vorticity.

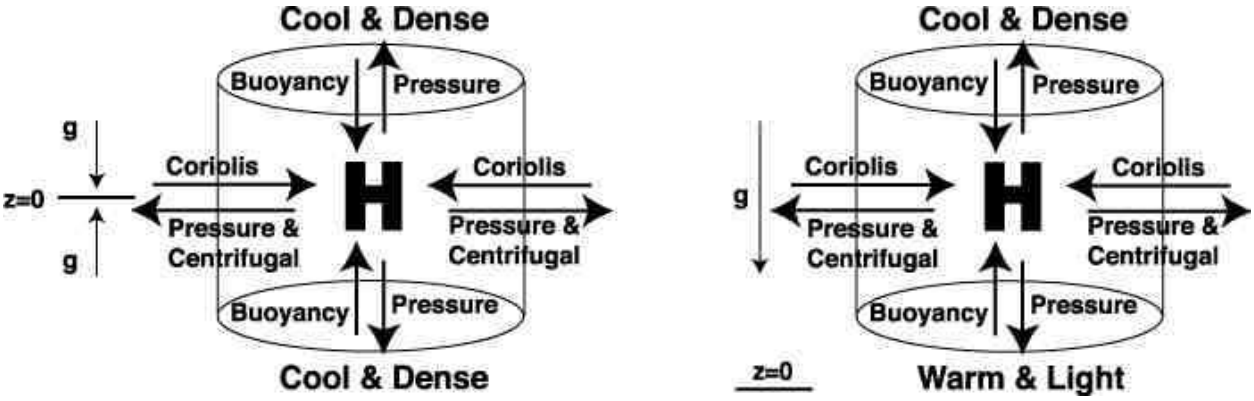

Fig. 2.— Balance of forces in an anticyclone with Rossby number less than unity.

We now turn to the balance of forces in a 3D vortex. In any horizontal plane, the centrifugal force always points radially outward from the vortex center, whereas the Coriolis force points outward for cyclones and inward for anticyclones. When the Rossby number is much greater than unity, the Coriolis force is negligible. The outward centrifugal force must be balanced by an inward pressure force; such vortices must have low-pressure cores. When the Rossby number is less than unity, the centrifugal force is small and the Coriolis force is balanced by the pressure force. Cyclones must have low-pressure cores and anticyclones must have high-pressure cores.

In the vertical direction, the only force that can balance the pressure force is buoyancy. Figure 2a shows the balance of forces in a low Rossby number anticyclone that is vertically centered on the midplane, whereas figure 2b shows the same for an anticyclone located completely above the midplane. In the first case, the high-pressure anticyclone must have cool, dense lids to provide a buoyant force toward the midplane that balances the pressure force away from the midplane. In the second case, the top lid (i.e., the one farthest from the midplane) must be cool and dense, whereas the bottom lid (i.e., the one closest to the midplane) must be warm and light. These thermal lids will be weakened or destroyed either by radiation of heat or turbulent erosion. Thus, a vertical flow must develop within the vortex to maintain the lids. For a high-pressure anticyclone centered on the midplane, gas will rise away from the midplane, adiabatically expanding and cooling. At the lids, the gas diverges outward and recirculates back toward the midplane along the edges of the vortex. For an anticyclone that is completely above the midplane, gas will rise (sink) toward the top (bottom) lid, where it will expand and cool (compress and heat-up).

We can use the arguments in this section to derive simple scaling relationships for the vortex flow variables, which will then guide us in making further approximations to the fluid equations. We decompose each flow variable into a time-independent, axisymmetric component describing the base disk flow, which we will denote with overbars, and a time-dependent component describing the vortex flow, which we will denote with tildes (e.g., $\rho = \bar{\rho} + \tilde{\rho}$, $p = \bar{p} + \tilde{p}$). As discussed in the previous subsection, we assume that the horizontal vortex flow is subsonic: $\tilde{v}_\perp / c_s \sim \epsilon < 1$. If the Rossby number is of order unity or less, then the horizontal pressure force must be of the same order as the Coriolis force (geostrophic balance): $\tilde{p}/\bar{\rho}\Lambda_r \sim 2\Omega\tilde{v}_\perp$, where $\tilde{p}$ is the pressure perturbation associated with the vortex, and $\bar{\rho}$ is the mean density. Using (2-1a) and (2-6), one can show that the pressure perturbation in the vortex must scale as: $\tilde{p}/\bar{p} \sim \epsilon^2/Ro$. We also assume the vertical buoyancy force is of order the vertical pressure gradient: $g_z\tilde{T}/\bar{T} \sim \tilde{p}/\bar{\rho}H$, which leads to the temperature fluctuation having the same scaling as the pressure fluctuation: $\tilde{T}/\bar{T} \sim \tilde{p}/\bar{p}$. Because of the ideal gas law, this implies that density fluctuations also have the same scaling. The scaling for the vertical velocity is set by the maintenance of temperature perturbations in the thermal

lids. In the temperature equation, temperature fluctuations are created via pressure-volume work: $\tilde{v}_z \bar{T}(d\bar{s}/dz)/C_v$, where $\tilde{v}_z$ is the vertical velocity, $\bar{s}$ is the mean entropy profile, and C_v is the heat capacity at constant volume. The destruction process is either radiative heating/cooling, $\tilde{T}/\tau_{cool}$, where τ_{cool} is a characteristic cooling time; or turbulent advection, $\tilde{T}/\tau_{eddy} \sim \tilde{v}_\perp \tilde{T}/\Lambda_r$, where τ_{eddy} is a characteristic eddy diffusion time. If the vortex flow is smooth and laminar, then we balance pressure-volume work with thermal cooling to obtain the scaling: $\tilde{v}_z \sim (\epsilon^2/Ro)H/\tau_{cool}$. Thus, if the vortex is laminar and the cooling time is long, the vertical velocity can be quite small. On the other hand, if the vortex flow is highly turbulent, we balance pressure-volume work and the turbulent advection of heat to obtain the scaling: $\tilde{v}_z \sim \epsilon^2$. These scaling relationships are summarized in Table 2.

3. FLUID EQUATIONS AND NUMERICAL METHOD

3.1. Cartesian and anelastic approximations

Motivated by the scalings discussed in the previous section, we focus on subsonic, compact vortices that have horizontal extent Λ_r comparable to the vertical scale height H, which is much smaller than the distance r to the protostar: $\Lambda_r/H \sim \epsilon/Ro \lesssim 1$ and $\Lambda_r/r \sim \epsilon\delta/Ro \ll 1$. This allows us to make two key approximations to the hydrodynamics.

The first simplification we make is the Cartesian approximation (Goldreich & Lynden-Bell 1965): we simulate the hydrodynamics only within a small patch of the disk ($\Delta r \ll r_0, \Delta\phi \ll 2\pi$) that co-rotates with the gas at some fiducial radius r_0. We map this patch of the disk onto a Cartesian grid: $r - r_0 \to x$, $r_0(\phi - \phi_0) \to y$, $z \to z$, $v_r \to v_x$, $v_\phi \to v_y$, and $v_z \to v_z$. The background shear and mean thermodynamic variables have radial gradients that vary on the length scale r which is much larger than the characteristic size of a subsonic vortex. For example, let $\bar{q}$ represent any background disk variable; then the variation $\delta\bar{q}$ over the size of a vortex is: $\delta\bar{q}/\bar{q} \sim (\partial \ln \bar{q}/\partial r)\Lambda_r \sim \Lambda_r/r \ll 1$. This allows us to neglect radial gradients of the mean thermodynamic variables and to linearize the Keplerian shear flow. The time-independent, axisymmetric base Keplerian flow in the rotating frame, which we denote with overbars, is then:

$$\bar{\mathbf{v}} = -\tfrac{3}{2}\Omega_0 x \hat{\mathbf{y}}, \tag{3-1a}$$

$$\bar{T} = T_0, \tag{3-1b}$$

$$\bar{\rho} = \rho_0 \exp(-z^2/2H_0^2), \tag{3-1c}$$

$$\bar{p} = p_0 \exp(-z^2/2H_0^2), \tag{3-1d}$$

$$\bar{s} = \mathcal{R} z^2/2H_0^2, \tag{3-1e}$$

where $\bar{T}$, $\bar{\rho}$, $\bar{p}$, $\bar{s}$ are the mean temperature, density, pressure, and entropy, respectively, which depend only on the vertical coordinate z. We have defined: $\Omega_0 \equiv \Omega_K(r_0)$, $p_0 \equiv \rho_0 \mathcal{R} T_0$, $H_0^2 \equiv \mathcal{R} T_0 / \Omega_0^2$, and $\mathcal{R}$ is the gas constant. The errors in making this Cartesian approximation are of order $\mathcal{O}(\epsilon\delta, \delta^2)$. Note that neglecting radial gradients of the background disk properties effectively filters out Rossby waves (which require a gradient in the background vorticity) and large-scale baroclinic instabilities. Our rationale for this is that if there were indeed large-scale baroclinic instabilities, they would produce large, supersonic vortices which would rapidly decay from radiation of acoustic waves and shocks.

The second simplification we make is the anelastic approximation: all variables are expanded in powers of the Mach number (e.g., $\mathbf{v} = \epsilon(\bar{\mathbf{v}} + \tilde{\mathbf{v}}) + \ldots$; $p = \bar{p} + \epsilon^2 \tilde{p} + \ldots$; $\rho = \bar{\rho} + \epsilon^2 \tilde{\rho} + \ldots$). These expansions are then substituted into the Euler equations, and terms are grouped by like powers of ϵ; we keep only the first-order corrections (Barranco et al. 2000). The anelastic approximation has been used extensively in the study of deep, subsonic convection in planetary atmospheres (Ogura & Phillips 1962; Gough 1969) and stars (Gilman & Glatzmaier 1981; Glatzmaier & Gilman 1981a,b). One of the consequences of this approximation is that the total density is replaced by the time-independent mean density in the mass continuity equation, which has the effect of filtering high-frequency acoustic waves and shocks, but allowing slower wave phenomena such as internal gravity waves. The errors in making the anelastic approximation are of order $\mathcal{O}(\epsilon^2)$. The anelastic Euler equations in the co-rotating frame are:

$$\tilde{p} = \bar{\rho}\mathcal{R}\tilde{T} + \tilde{\rho}\mathcal{R}\bar{T}, \tag{3-2a}$$

$$0 = \nabla \cdot (\bar{\rho}\mathbf{v}), \tag{3-2b}$$

$$\frac{d\mathbf{v}}{dt} = -2\Omega_0 \hat{\mathbf{z}} \times \mathbf{v} + 3\Omega_0^2 x \hat{\mathbf{x}} - \frac{1}{\bar{\rho}}\nabla\tilde{p} - \frac{\tilde{\rho}}{\bar{\rho}}\Omega_0^2 z \hat{\mathbf{z}}, \tag{3-2c}$$

$$\frac{dT}{dt} = -(\gamma - 1)T\,(\nabla \cdot \mathbf{v}) - (T - \bar{T})/\tau_{cool}(z), \tag{3-2d}$$

where the advective derivative is defined as $d/dt \equiv \partial/\partial t + \mathbf{v} \cdot \nabla$, and where $\gamma \equiv C_P/C_V$ is the ratio of specific heats. Equation (3-2b) is the crux of the anelastic approximation: the time-derivative has dropped out of the mass continuity equation, which effectively filters out all acoustic phenomena. The terms on the right hand side of the momentum equation (3-2c) are: the Coriolis force, the tidal force (the remainder after balancing the radial component of the protostellar gravity and the centrifugal non-inertial force), the pressure force, and the buoyancy force. In equation (3-2d), the first term on the right hand side is pressure-volume work (which is reversible) and the second term represents a simplified model of cooling or thermal relaxation. In the limit where the cooling time τ_{cool} is infinitely long, one can show that the temperature equation is equivalent to entropy being advectively conserved: $ds/dt = 0$.

3.2. Spectral expansions and boundary conditions

In this and the following subsection, we briefly describe the numerical method; a more detailed presentation can be found in Barranco & Marcus (2004). We solve the Euler equations (3-2) with a spectral method; that is, each variable is represented as a finite sum of basis functions multiplied by spectral coefficients (Gottlieb & Orszag 1977; Marcus 1986; Canuto et al. 1988; Boyd 1989). The choice of basis functions for each direction is guided by the corresponding boundary conditions. The equations are autonomous in the azimuthal coordinate y, so it is reasonable to assume periodic boundary conditions in this direction. However, the equations explicitly depend on the radial coordinate x because of the linear background shear. We adopt "shearing box" boundary conditions: $\tilde{q}(x+L_x, y-(3/2)\Omega_0 L_x t, z, t) = \tilde{q}(x, y, z, t)$, where $\tilde{q}$ represents any of $\tilde{\mathbf{v}}$, $\tilde{p}$, $\tilde{T}$, etc. In practice, we rewrite the equations (3-2) in terms of quasi-Lagrangian or shearing coordinates that advect with the background shear (Goldreich & Lynden-Bell 1965; Marcus & Press 1977; Rogallo 1981): $t' \equiv t$, $x' \equiv x$, $y' \equiv y + (3/2)\Omega_0 x t$, and $z' \equiv z$. In these new coordinates, the radial boundary conditions become: $\tilde{q}(x'+L_x, y', z', t') = \tilde{q}(x', y', z', t')$. That is, shearing box boundary conditions are equivalent to periodic boundary conditions in the shearing coordinates. Physically, this means that the periodic images at different radii are not fixed, but advect with the background shear.

In the shearing coordinates, the equations are autonomous in both x' and y' (although they now explicitly depend on t'), making a Fourier basis the natural choice for the spectral expansions in the horizontal directions:

$$\tilde{q}(x', y', z', t') = \sum_{\mathbf{k}} \hat{q}_{\mathbf{k}}(t') e^{ik'_x x'} e^{ik'_y y'} \phi_n(z'), \tag{3-3}$$

where $\tilde{q}$ is any variable of interest, $\{\hat{q}_{\mathbf{k}}(t')\}$ is the set of spectral coefficients, and $\mathbf{k} = \{k'_x, k'_y, n\}$ is the set of wavenumbers. We have implemented the simulations with two different sets of basis functions for the spectral expansions in the vertical direction, corresponding to two different sets of boundary conditions:

(i) For the truncated domain $-L_z \le z \le L_z$, we use Chebyshev polynomials: $\phi_n(z) = T_n(z/L_z) \equiv \cos(n\xi)$, where $\xi \equiv \cos^{-1}(z/L_z)$. We apply the condition that the vertical velocity vanish at the top and bottom boundaries: $\tilde{v}_z(x, y, z = \pm L_z, t) = 0$.

(ii) For the infinite domain $-\infty < z < \infty$, we use rational Chebyshev functions: $\phi_n(z) = \cos(n\xi)$ (for $\tilde{v}_x$, $\tilde{v}_y$, $\tilde{\omega}_z$, and all the thermodynamic variables) or $\phi_n(z) = \sin(n\xi)$ (for $\tilde{v}_z$, $\tilde{\omega}_x$ and $\tilde{\omega}_y$), where $\xi \equiv \cot^{-1}(z/L_z)$. In this context, L_z is no longer the physical size of the box, but is a mapping parameter; exactly one half of the grid points are within $|z| \le L_z$, whereas the other half are widely spaced in the region $L_z < |z| < \infty$. No explicit boundary

conditions on the vertical velocity are necessary when we solve the equations on the infinite domain because the $\phi_n(z) = \sin(n\xi)$ basis functions individually decay to zero at large z.

3.3. Brief description of the numerical method

The equations are integrated forward in time with a fractional step method: the nonlinear advection terms are integrated with an explicit second-order Adams-Bashforth method, and the pressure step is computed with a semi-implicit second-order Crank-Nicholson method. The time integration scheme is overall globally second-order accurate. Unlike finite-difference methods, spectral methods have no inherent grid dissipation; energy cascades to smaller and smaller size scales via the nonlinear interactions, where it can "pile-up" and potentially degrade the convergence of the spectral expansions. We employ a ∇^8 hyperviscosity or low-pass filter every timestep to damp the energy at the highest wavenumbers.

Different horizontal Fourier modes interact only through the nonlinear advective terms; once these terms are computed, the horizontal Fourier modes can be decoupled. This motivated us to parallelize the code: each processor computes on a different block of data in horizontal Fourier wavenumber space. Parallelization is implemented with Message Passing Interface (MPI) on the IBM Blue Horizon and IBM Datastar at the San Diego Supercomputer Center, typically using between 64 and 512 processors. Wall-clock time scales inversely with number of processors, indicating near-optimal parallelism; timing analyses are presented in Barranco & Marcus (2004).

4. RESULTS OF NUMERICAL SIMULATIONS

In the following presentation of the numerical simulations, we define a system of units such that $\Omega_0 = H_0 = \rho_0 = 1$, $c_{s0} = \Omega_0 H_0 = 1$, and $RT_0 = c_{s0}^2 = 1$. With these units, the Mach number of a computed flow is $\epsilon = \max(\tilde{v})$ and the Rossby number is $Ro = (1/2)\max(\tilde{\omega}_z)$. All of the simulations presented in this section were computed with $\tau_{cool} \rightarrow \infty$. We will explore the effects of cooling in future work.

4.1. Vortex initialization

The key to initializing a 3D vortex is to guess a vorticity configuration that is as close to equilibrium as possible so that the initial accelerations are small and the flow can slowly relax to its true equilibrium; otherwise, the vortex will be ripped apart by large accelerations. As

discussed in Section 2.1, Moore & Saffman (1971) and Kida (1981) analytically determined exact steady-state solutions for 2D elliptical vortices of uniform vorticity embedded in a linear background shear. We use these 2D solutions as the starting point for constructing initial conditions for 3D vortices. We set $\tilde{v}_z$ and $\partial\tilde{v}_z/\partial t$ to be initially zero, which implies that the horizontal velocity fields at different heights are initially uncoupled and can be initialized independently. At each height, we construct a 2D elliptical vortex of constant $\tilde{\omega}_z$ whose strength and shape satisfy equation (2-4) so that $\partial\tilde{\mathbf{v}}_\perp/\partial t = 0$. The ellipses at different heights do not necessarily have to have the same size, shape, or strength; in the following subsections, we will describe two different ways of "stacking" 2D elliptical vortices to create a 3D vortex. The anticyclonic core of the vortex is surrounded by a larger elliptical "halo" of weak cyclonic vorticity so that the net circulation in each horizontal plane equals zero: $\Gamma \equiv \int_A \tilde{\omega}_z dxdy = 0$. We define a 2D streamfunction $\tilde{\psi}$ such that: $\tilde{\mathbf{v}}_\perp \equiv \nabla_\perp \times \tilde{\psi}\hat{\mathbf{z}}$ and $\tilde{\omega}_z = -\nabla_\perp^2\tilde{\psi}$. Thus, once $\tilde{\omega}_z$ is initialized at each height, we invert a 2D Poisson operator to obtain the streamfunction, which in turn generates the horizontal velocity field. The 2D pressure field can be found by taking the horizontal divergence of the horizontal momentum equation and inverting another 2D Poisson operator. The pressure will likely have a nonzero vertical gradient, which if left unbalanced, will lead to large vertical accelerations. We still have one more degree of freedom: we initialize the temperature field so that the buoyancy force exactly balances the vertical pressure force:

$$\tilde{T} = \frac{T_0}{\Omega_0^2 z}\frac{\partial(\tilde{p}/\bar{\rho})}{\partial z}. \tag{4-1}$$

Thus, all three components of the momentum equation are exactly balanced and the accelerations are all initially zero: $\partial\tilde{\mathbf{v}}/\partial t = 0$. Of course, only under very special circumstances would this procedure just so happen to also exactly balance the temperature equation. In general, $\partial\tilde{T}/\partial t \neq 0$ initially, leading to an immediate evolution of the temperature field. Vertical motions will then be generated by the temperature changes through the buoyancy force, and these vertical velocities will then couple the horizontal motions at different heights.

4.2. Tall, columnar vortex

For our first initial condition, we constructed the simplest 3D analog of a 2D vortex: an "infinite" column created by stacking identical 2D elliptical vortices at every height. The vertical vorticity $\tilde{\omega}_z$, horizontal velocity $\tilde{\mathbf{v}}_\perp$ and enthalpy $\tilde{p}/\bar{\rho}$ were all independent of height, and the temperature perturbation was set identically to zero inside and outside the vortex. This initial condition was an exact equilibrium solution of the momentum and temperature equations: $\partial\tilde{\mathbf{v}}/\partial t = \partial\tilde{T}/\partial t = 0$. However, it turned out that this quasi-2D vortex is unstable to small perturbations in 3D.

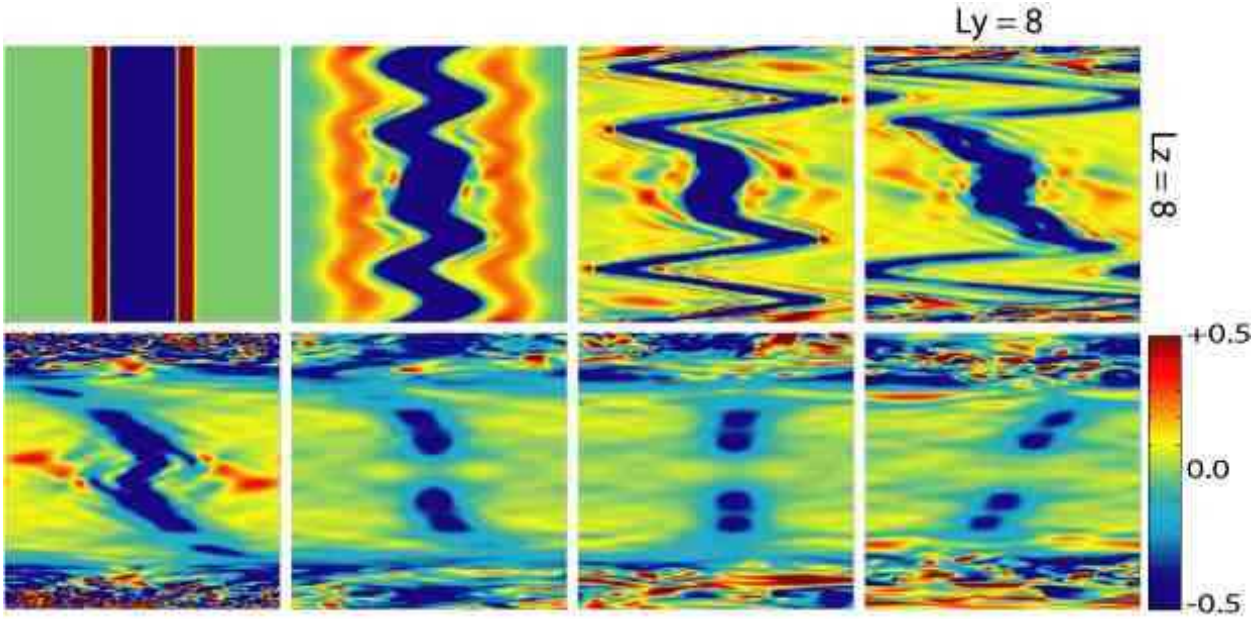

Fig. 3.— Tall, columnar vortex: $y-z$ slices at $x=0$ of the z-component of vorticity $\tilde{\omega}_z$. Blue = anticyclonic vorticity; red = cyclonic vorticity. The initial elliptical column had aspect ratio $\chi = 4$ and vorticity $\tilde{\omega}_z = 0.625$, corresponding to a Rossby number $Ro = 0.3125$. The times corresponding to each frame are: $t/\tau_{orb} = 0.0, 2.1, 4.2, 6.4, 51, 102, 153, 204$.

Figure 3 shows the evolution of a perturbed columnar vortex. The domain dimensions for the simulation were $(L_x, L_y, L_z) = (2, 8, 8)$, and the numbers of grid points/spectral coefficients along each direction were $(N_x, N_y, N_z) = (64, 256, 256)$. The vertical velocity was forced to vanish on the top and bottom boundaries of the domain: $\tilde{v}_z(z = \pm 4) = 0$. The minor and major axes (along the x and y directions, respectively) of the elliptical column were $(\Lambda_x, \Lambda_y) = (0.5, 2.0)$, corresponding to an aspect ratio of $\chi = 4$. The magnitude of the anticyclonic vorticity in the core of the vortex was $\tilde{\omega}_z = 0.625$, corresponding to a Rossby number $Ro = 0.3125$. The maximum value of the initial horizontal speed was $\tilde{v}_{\perp,max} = 0.12$. In order to investigate the stability of the tall column, we did not stack the 2D ellipses exactly on top of one another, but instead offset the locations of their centers in the radial direction so that the centerline of the column had coordinates: $\{x_c, y_c\} = \{A \sin(2\pi m z/L_z), 0\}$, where $A = 0.1\Lambda_r = 0.05$ and $m = 4$.

Because there is initially no vertical velocity or vertical enthalpy gradient, the different layers of the vortex do not communicate with each other, and tend to drift apart, carried by the ambient shear. As the vortex lines are stretched, a restoring force is generated which tries to vertically realign the vortex. The restoring force is partially successful in realigning a segment of the vortex around the midplane, but the parts of the vortex away from the midplane are sheared away, leaving a vertically truncated vortex straddling the midplane. Later, it appears that this truncated vortex goes through another instability and splits into two independent vortices above and below the midplane. These off-midplane vortices survive for well over a hundred orbits around the disk.

From this simulation, it is clear that vertical stratification plays a key role in the vortex dynamics. The vertical component of the protostellar gravity is $g_z = \Omega_0^2 z$ and the Brunt-Väisälä frequency is $\omega_{BV} \approx \Omega_0 |z|/H_0$. Far from the midplane $|z| > H_0$ the gas in the disk is strongly stratified ($Fr \equiv \tau_{BV}/\tau_{vor} < 1$), which inhibits the development of vertical motions which would couple the layers together. Thus, far from the midplane, the different layers of the vortex are free to drift apart, carried by the ambient shear. In contrast, there is virtually no stratification in the immediate vicinity of the midplane ($Fr > 1$), and a vertical flow rapidly develops to couple the layers together and prevent the ambient shear from ripping apart the vortex.

4.3. Finite-height cylindrical vortex

Motivated by the fact that tall, columnar vortices cannot maintain vertical coherence over more than a couple scale heights, we constructed a short, columnar vortex that was vertically centered on the disk midplane. We initialized a 2D ellipse in the midplane whose

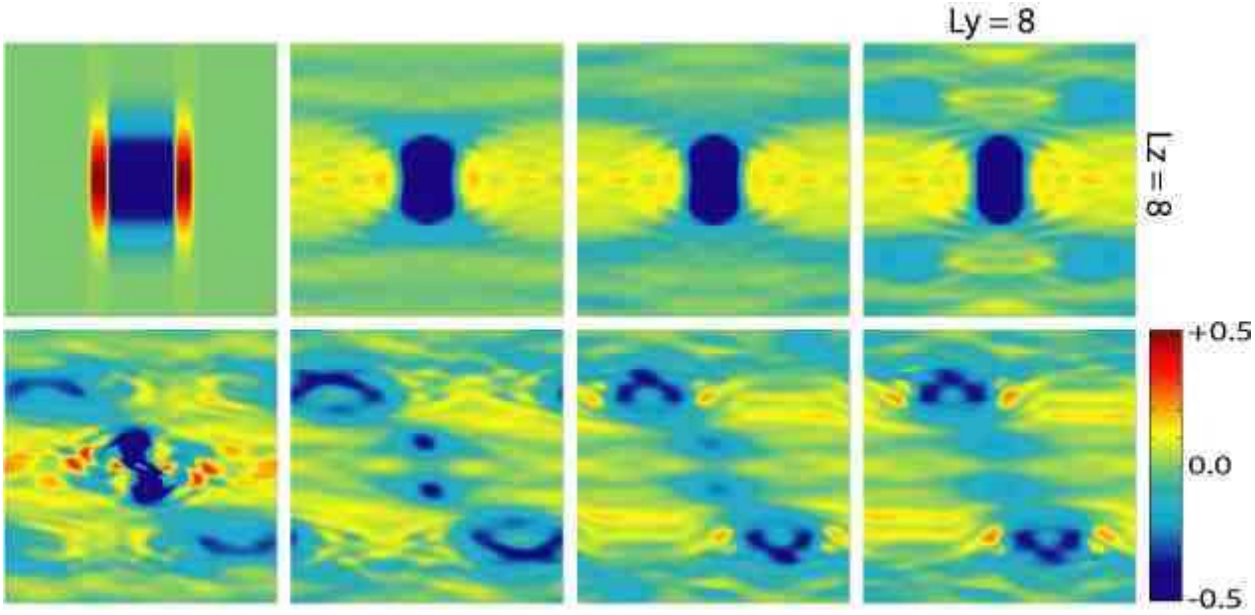

Fig. 4.— Finite-height cylindrical vortex: $y-z$ slices at $x=0$ of the z-component of vorticity $\tilde{\omega}_z$. Blue = anticyclonic vorticity, red = cyclonic vorticity. The initial elliptical cylinder had aspect ratio $\chi = 4$ and vorticity $\tilde{\omega}_z = 0.625$, corresponding to a Rossby number $Ro = 0.3125$. The time between frames is $\Delta t/\tau_{orb} \approx 60$.

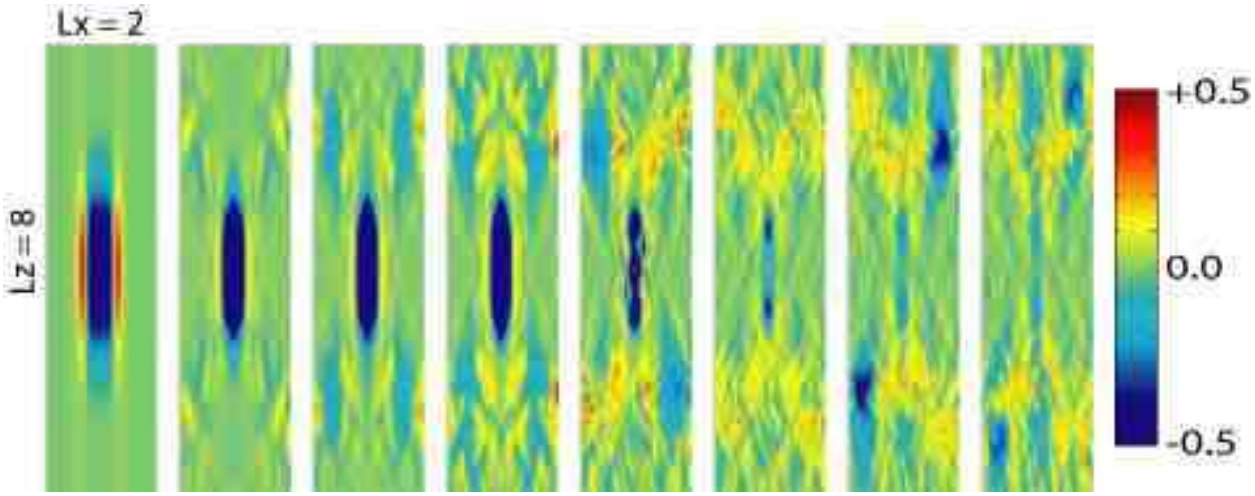

Fig. 5.— Finite-height cylindrical vortex: $x-z$ slices at $y=0$ of the z-component of vorticity $\tilde{\omega}_z$. Blue = anticyclonic vorticity, red = cyclonic vorticity. The initial elliptical cylinder had aspect ratio $\chi = 4$ and vorticity $\tilde{\omega}_z = 0.625$, corresponding to a Rossby number $Ro = 0.3125$. The time between frames is $\Delta t/\tau_{orb} \approx 60$.

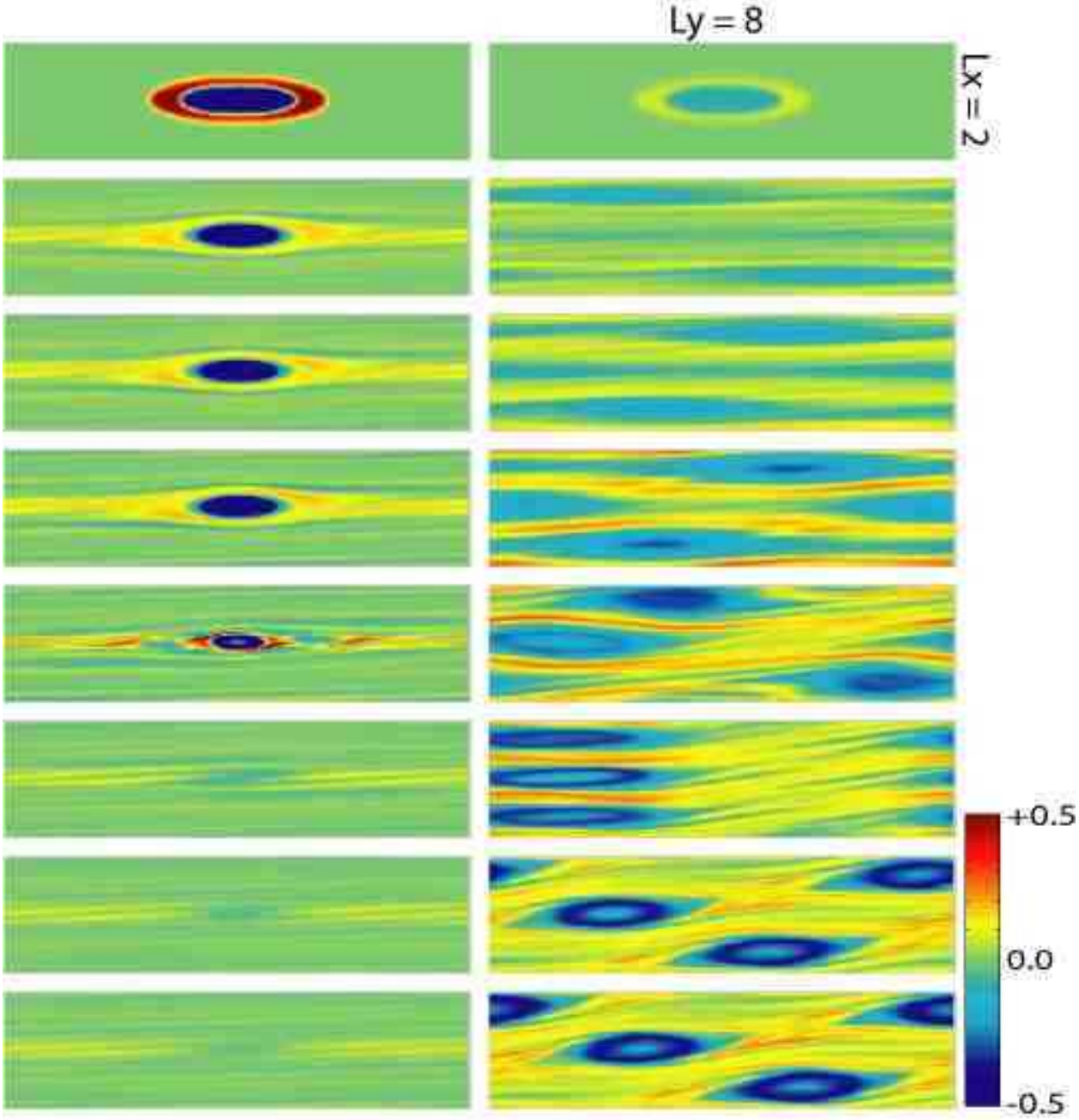

Fig. 6.— Finite-height cylindrical vortex: x–y slices at $z=0$ (first column) and $z=2$ (second column) of the z-component of vorticity $\tilde{\omega}_z$. Blue = anticyclonic vorticity, red = cyclonic vorticity. The initial elliptical cylinder had aspect ratio $\chi = 4$ and vorticity $\tilde{\omega}_z = 0.625$, corresponding to a Rossby number $Ro = 0.3125$. The time between frames is $\Delta t/\tau_{orb} \approx 60$.

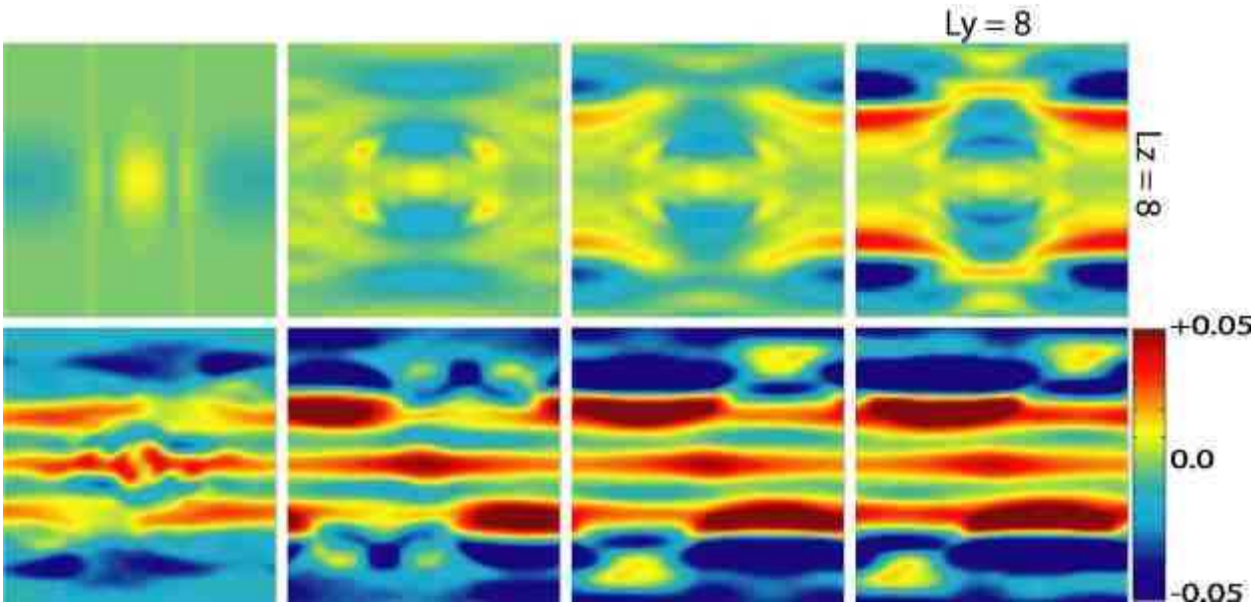

Fig. 7.— Finite-height cylindrical vortex: y–z slices at $x=0$ of the temperature perturbation $\tilde{T}$. Blue = cool, red = warm. The initial elliptical cylinder had aspect ratio $\chi = 4$ and vorticity $\tilde{\omega}_z = 0.625$, corresponding to a Rossby number $Ro = 0.3125$. The time between frames is $\Delta t/\tau_{orb} \approx 60$.

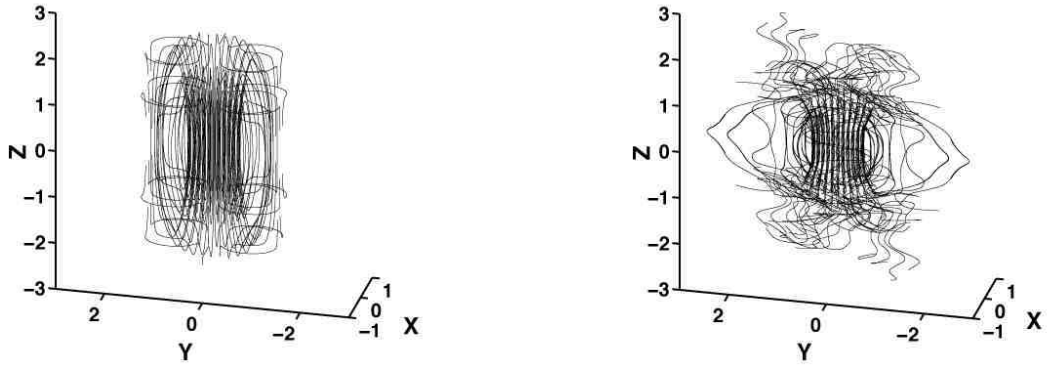

Fig. 8.— Vortex lines for finite-height cylindrical vortex , at times $t/\tau_{orb} = 0, 170$.

minor and major axes were $(\Lambda_x, \Lambda_y) = (0.5, 2.0)$, corresponding to an aspect ratio of $\chi = 4$. The magnitude of the vorticity in the core of the vortex was $\tilde{\omega}_z(z = 0) = 0.625$ at the midplane, corresponding to a Rossby number $Ro = 0.3125$. The maximum value of the initial horizontal speed was $\tilde{v}_{\perp,max} = 0.12$. The vorticity was extended off the midplane according to a Gaussian profile:

$$\tilde{\omega}_z(z) = \tilde{\omega}_z(0) e^{-z^2/2H_0^2}, \tag{4-2}$$

where the scale height of the vorticity was the same as the pressure scale height. For an anticyclone with $Ro \lesssim 1$, the inward Coriolis force is somewhat more dominant than than the outward centrifugal force, and the vortex must be a region of high pressure for horizontal equilibrium (see Figure 2). The high-pressure core extends only over a finite height, so that there is a vertical pressure force away from the midplane. In order for the vortex to be in vertical equilibrium, there must be cool, dense lids which provide a buoyancy force directed toward the midplane.

Figures 4 and 5 show the time evolution of the z-component of the vorticity in vertical slices $y{-}z$ at $x{=}0$ and $x{-}z$ at $y{=}0$. Figure 6 shows the z-component of the vorticity in two different horizontal slices $x{-}y$ at $z{=}0$ (first column) and $z{=}2$ (second column). Figure 7 shows vertical slices $y{-}z$ at $x{=}0$ of the temperature perturbation. The time between frames in all these figures is $\Delta t/\tau_{orb} \approx 60$. These results were computed with the infinite vertical domain version of the simulation: the horizontal dimensions were $(L_x, L_y) = (2, 8)$, and the vertical mapping parameter was $L_z = 4$. The numbers of spectral modes along each direction were $(N_x, N_y, N_z) = (64, 256, 256)$. The three components of the momentum equation were exactly satisfied initially, but the energy equation was out of equilibrium from the start. The temperature field slowly evolved, generating a small vertical velocity which then coupled the horizontal layers together. After approximately a few dozen τ_{orb}, the vertically truncated vortex settled into a new, quasi-equilibrium (see frames 2-4 in Figures 4–7) that changed very little over the course of a couple hundred orbits through the disk. Figure 8 shows vortex lines for the initial condition and for the quasi-equilibrium steady-state at $t/\tau_{orb} = 170$.

We thought we had indeed found a stable steady-state, but surprisingly the vortex suffered a dramatic instability which ultimately resulted in the complete destruction of the vortex in the midplane (see frame 5 in Figures 4–7). The initial condition was symmetric with respect to the midplane, and the equations of motion (3-2) should have preserved this symmetry. However, the instability clearly had an antisymmetric component. We decomposed the flow into its symmetric and antisymmetric parts. Figure 9 shows the maximum absolute value of the antisymmetric part of the z-component of vorticity as a function of time. Initially, it was very close to zero, but grew from numerical round-off errors. Eventually, a linear eigenmode emerged out of this numerical antisymmetric noise. The structure

of the mode preserved its spatial form for over ten orders of magnitude of growth, proving that it is indeed a linear instability. The e-folding time of the exponential growth was a few τ_{orb}.

Thus, although the instability itself had a fast timescale, the vortex appeared to survive for a long time in its quasi-equilibrium state because a sufficient amount of numerical noise had to be generated in the antisymmetric modes to seed the eigenmode. In simulations in which we enforced symmetry about the midplane of the disk, the truncated vortex survived for longer periods of time, but eventually succumbed to slower symmetric instabilities.

4.4. Off-midplane anticyclonic vortices and cyclonic azimuthal bands

A closer inspection of frames 4–8 in Figures 4–7 revealed coherent regions of anticyclonic vorticity a couple scale heights above and below the midplane of the disk. These new vortices formed *before* the vortex in the midplane succumbed to the antisymmetric instability, and survived indefinitely in our simulations (over 400 orbits). The highly stratified disk supports neutrally stable internal gravity waves. As a midplane vortex slowly relaxes to its quasi-equilibrium, it oscillates and excites internal gravity waves which travel obliquely off the midplane of the disk. As the waves propagate off the midplane, conserving their flux of kinetic energy, the velocity and temperature perturbations increase, the waves break, and baroclinicity turns these perturbations into vorticity. The anticyclonic shear of the disk stretches the cyclonic vorticity into sheets or bands, whereas the anticyclonic vorticity perturbations roll-up into new, coherent vortices. Like the midplane-centered vortices, these off-midplane vortices are also high-pressure anticyclones. For a vortex in the upper half of the disk, the high-pressure core is balanced by a cool, dense top lid which pushes downward, and a warm, low-density bottom lid which pushes upward. These lids can easily be seen in frames 6–8 in Figure 7. The density and temperature of these lids are maintained by the vertical motions within the vortex: rising (falling) motion adiabatically cools (heats) the stably-stratified fluid.

There are two intriguing features of these off-midplane vortices. First, the three vortices approach one another and strongly interact, stretching and squeezing each other. Clearly, these are robust features that are able to survive for hundreds of orbits despite strong perturbations. One can see thin bands of cyclonic vorticity that keep the vortices separated; the bands are most prominent at closest approach (see the sixth frame down in column 2 of Figure 6). Second, the off-midplane vortices appear to be "hollow" in the sense that the maximum vorticity does not occur at the center of the vortex, but on the rim. The Great Red Spot is probably the most famous example of a hollow vortex; the center of the GRS may,

in fact, be weakly counter-rotating (Marcus 1993). It is still a mystery as to how the GRS maintains its hollowness. Numerical simulations of 2D hollow vortices show that they are violently unstable; the low-vorticity fluid in the core switches places with the high-vorticity fluid on the rim, resulting in a vortex whose vorticity profile is centrally peaked (Youssef 2000; Shetty et al. 2004). Here in our 3D simulations, hollow vortices are apparently stable.

In order to get a better understanding on the structure of these off-midplane vortices, we isolated one of them and used it as a new initial condition. In this simulation, there is no vortex in the midplane, and except for the lone off-midplane vortex at $z = 2$, the rest of the domain is pure Keplerian with no initial pressure, temperature, or density perturbations anywhere else. Figure 10 shows the evolution of this isolated off-midplane vortex. In frame 2 ($\approx 42\tau_{orb}$), one can clearly see anticyclonic bands forming. By frame 4 ($\approx 126\tau_{orb}$), the bands have rolled up and coalesced into two new vortices. The final state once again has 3 off-midplane vortices. Most importantly, this simulation shows that that the vorticity for these new vortices did not come from the redistribution of vorticity remnants from the destruction of a midplane-centered vortex, but out of some new instability in the stratified region of the disk. In a future paper, we will focus on the mechanisms for vorticity generation and the sources of energy for these off-midplane vortices.

4.5. Angular momentum transport

One of the prime motivations for interest in coherent vortices in protoplanetary disks is whether they can transport sufficient angular momentum outward so that mass can continue to accrete onto the growing protostar. Following Balbus & Hawley (1998), one can relate the correlations of the fluctuating perturbation velocities (whether from turbulence or coherent vortices) to the eddy-viscosity model:

$$\alpha = \langle \tilde{v}_x \tilde{v}_y \rangle / c_s^2, \tag{4-3}$$

where we have defined a density-weighted average $\langle \tilde{v}_x \tilde{v}_y \rangle \equiv \int \bar{\rho} \tilde{v}_x \tilde{v}_y dx dy dz / \int \bar{\rho} dx dy dz$. For an isolated vortex that is fore-aft symmetric (e.g., $\tilde{v}_x$ is antisymmetric across the x-axis, symmetric across the y-axis and $\tilde{v}_y$ is symmetric across the x-axis, antisymmetric across the y-axis), one can show that the velocity correlation defined above vanishes; these symmetries must be broken in order to have non-zero transport. However, if the disk is filled with vortices, vortex-vortex interactions and mergers can break the fore-aft symmetry, allowing for angular momentum transport.

In Figure 11, we plot the velocity correlations for the long-term simulation of a finite-height midplane vortex settling into a quasi-equilibrium, going unstable, and new, off-

midplane vortices forming. In the first panel, we plot the instantaneous correlations, which are highly time-dependent. Note that the correlations are both positive (outward transport of angular momentum) and negative (inward transport). The strong positive and negative spikes in this raw data are due to the interactions of the off-midplane vortices when they are at closest approach (see frame 6 in column 2 of Figure 6). In the second panel, we present a moving average (rectangular window with width $10\tau_{orb}$) of the same data. The smoothed correlations are always positive (outward transport of angular momentum) and correspond to an average $\alpha \approx 10^{-5}$.

One must be careful when extrapolating the results of angular momentum transport in a local patch of the disk to the global transport in a whole disk. Our simulations are periodic in the azimuthal direction y, implying that there is a periodic array of vortices around the protostar, with azimuthal separation L_y. However, vortices that are at the same radius tend to merge, potentially reducing the effective rate of angular momentum transport. The simulation shown in Figure 10 shows that new vortices readily form in unoccupied radial bands. Thus, there is a competition between mergers, which reduce the number of vortices per radial band, and the formation mechanism that repopulates empty bands. In future simulations, we will extend the azimuthal domain to investigate multiple vortices per radial band and explore this competition between mergers and formation of new vortices.

5. SUMMARY & FUTURE WORK

This is the first *ever* calculation of long-lived, robust 3D vortices in protoplanetary disks. The fundamental fluid dynamics are governed by three key timescales (see Table 1): τ_{vor}, the orbital period of gas around the vortex core; τ_{orb}, the orbital period of the vortex around the protostar; and τ_{BV}, the Brunt-Väisälä period, or period of vertical oscillations (e.g., internal gravity waves) in a stably-stratified atmosphere. These three timescales are roughly of the same order because they are all determined by the protostellar gravity. However, the stratification in the disk has a strong spatial dependence, making the dynamics more complicated. The disk can roughly be divided into two regimes: a weakly stratified region in the immediate vicinity of the midplane ($|z| < H_0$, $Fr \equiv \tau_{BV}/\tau_{vor} > 1$), and a strongly stratified region away from the midplane ($|z| > H_0$, $Fr < 1$). Our numerical simulations have confirmed that stratification is a crucial ingredient for long-lived coherent vortices.

Earlier, 2D studies of vortices in disks (e.g., Adams & Watkins 1995; Bracco et al. 1998; Godon & Livio 1999, 2000) could not address the role of stratification. One way of interpreting their models is that a 2D vortex is a cross-section (in the midplane) of a tall column that penetrates through all the layers of the disk. Our numerical simulations (see

Figure 3) show that such columns, although they are *exact* steady-state equilibrium solutions to the 3D momentum and temperature equations, are unstable to 3D perturbations because stratification inhibits vertical motions which are needed to couple the layers together and lock the vertical alignment. Another possible interpretation of 2D analyses is that they capture the dynamics of vortices that are confined to the midplane of the disk. We initialized finite-height, cylindrical vortices straddling the midplane of the disk and allowed them to evolve into quasi-equilibria. These vortices were high-pressure anticyclones in which the inward Coriolis force balanced the outward pressure force. In the vertical direction, the vortex needed cool, dense lids to exert a buoyant force toward the midplane to balance the pressure force away from the midplane (see Figure 2). Long-term simulations of such vortices revealed that they too are unstable equilibria. We isolated an antisymmetric (with respect to the midplane) eigenmode that grew with an e-folding time of only a few orbital periods around the protostar. These vortices only seemed to last a long time because our initial conditions were symmetric with respect to the midplane, and the antisymmetric eigenmode was seeded only with numerical round-off error.

We confess that when we started this work, we too believed vortices in protoplanetary disks would be either quasi-2D "infinite" columns, or short truncated cylindrical vortices confined to the midplane of the disk. Surprisingly, our simulations revealed an unexpected third possibility: off-midplane vortices a few scale heights above and below the midplane. These vortices are also high pressure anticyclones. For a vortex in the upper half of the disk, the high-pressure core is balanced by a cool, dense top lid which pushes downward, and a warm, low-density bottom lid which pushes upward. The density and temperature of these lids are maintained by the vertical motions within the vortex: rising (falling) motion adiabatically cools (heats) a stably-stratified fluid (see Figure 2b). Simulations with no vertical gravity and/or those with barotropic equations of state will fail to find such vortices. Also, numerical calculations must have sufficient resolution to capture the thermal lids, which typically have thicknesses much smaller than the local pressure scale height.

Unlike the tall, columnar vortices and the finite-height cylindrical midplane vortices which we put in the disk by hand, the off-midplane vortices formed naturally from perturbations in the disk. For example, as a midplane vortex oscillated and relaxed toward its quasi-equilibrium (*not* the cataclysmic motions as it succumbed to the antisymmetric instability), it excited internal gravity waves which propagated away from the midplane, steepened, and broke, creating vorticity (a baroclinic effect). Regions of anticyclonic vorticity rolled-up and coalesced into new anticyclones, whereas regions of cyclonic vorticity were stretched into thin azimuthal bands and sheets by the ambient shear. In simulations where we had only one off-midplane vortex as an initial condition, new vortices reformed, filling every available radial band. These off-midplane vortices are robust, surviving indefinitely

in our simulations (over 400 orbits) despite countless close encounters and interactions with other vortices.

The symmetries of an isolated vortex preclude significant angular momentum transport. On the other hand, if the disk is filled with vortices that interact, merge and reform, those symmetries are broken and angular momentum can be transported at moderate rates. Thus, there is a competition between mergers of vortices that would reduce the number of vortices in a given radial band, and the formation of new vortices in unoccupied radial bands.

In order to understand how vortices are created and maintained, and whether they are isolated or fill the disk, it is necessary to determine the sources of energy and vorticity. Klahr & Bodenheimer (2003) demonstrated that a globally unstable radial entropy gradient in a protoplanetary disk excited Rossby waves which also broke into large-scale vortices. Because the length scale of the entropy gradient was of order r, the horizontal scales of the vortices were much larger than the thickness of the disk, and so the fluid velocities were supersonic. Acoustic waves and shocks rapidly drain the kinetic energy from such vortices. We plan to extend the radial domain in our simulations and relax the shearing box boundary conditions so that we may investigate radial gradients as well.

Coherent vortices located above and below the midplane will significantly affect the way dust settles into the midplane. Two-dimensional studies have shown that vortices are very efficient at capturing and concentrating dust particles (Barge & Sommeria 1995; Tanga et al. 1996; de la Fuente Marcos & Barge 2001). If the vortices are located off the midplane, will the dust grains be inhibited from settling into a thin, dense sublayer? If the vortices have a significant vertical velocity, will they be able to sweep up grains that have already settled into the midplane? We propose that the trapping of dust in off-midplane vortices is analogous to the formation of hail in the Earth's atmosphere; turbulent vertical velocities prevent grains from falling out of the vortices until they have grown to some critical mass. In future work, we plan to incorporate simple Lagrangian tracking of dust grains (de la Fuente Marcos et al. 2002), as well as two-fluid models (Cuzzi et al. 1993; Johansen et al. 2004).

P.S.M. thanks the support of NASA Grant NAG5-10664 and NSF Grant AST-0098465. J.A.B. thanks the NSF for support via a Graduate Student Fellowship while at Berkeley, and now with an Astronomy & Astrophysics Postdoctoral Fellowship (NSF Grant AST-0302146). He also thanks the support of the Kavli Institute for Theoretical Physics through NSF Grant PHY-9907949. Computations were carried out at the San Diego Supercomputer Center using an NPACI award. The authors would like to thank Berkeley graduate student Xylar Asay-Davis for preparing the animations that appear in the electronic version of this paper; and Professors Eugene Chiang, Geoff Marcy, and Andrew Szeri for useful comments

on the early manuscript.

REFERENCES

Adams, F. & Watkins, R. 1995, ApJ, 451, 314

Balbus, S. & Hawley, J. 1991, ApJ, 376, 214

—. 1998, Rev. Mod. Phys., 70, 1

Barge, P. & Sommeria, J. 1995, A&A, 295, L1

Baroud, C., Plapp, B., Swinney, H., & She, Z.-S. 2003, Phys. Fluids, 15, 2091

Barranco, J. & Marcus, P. 2004, J. Comp. Phys., submitted

Barranco, J., Marcus, P., & Umurhan, M. 2000, in Center for Turbulence Research – Proceedings of the 2000 Summer Program, 85–96

Blaes, O. & Balbus, S. 1994, ApJ, 421, 163

Boyd, J. 1989, Chebyshev and Fourier Spectral Methods (New York: Springer-Verlag)

Bracco, A., Provenzale, A., Spiegel, E., & Yecko, P. 1998, in Theory of Black Hole Accretion Disks, ed. M. Abramowicz, G. Bjornsson, & J. Pringle (Cambridge: Cambridge University Press), 254

Canuto, C., Hussaini, M., Quarteroni, A., & Zang, T. 1988, Spectral Methods in Fluid Dynamics (New York: Springer-Verlag)

Champney, J., Dobrovolskis, A., & Cuzzi, J. 1995, Phys. Fluids, 7, 1703

Chandrasekhar, S. 1960, Proc. Natl. Acad. Sci. USA, 46, 253

—. 1961, Hydrodynamic and Hydromagnetic Stability (New York: Dover)

Chavanis, P. 2000, A&A, 356, 1089

Cuzzi, J., Dobrovolskis, A., & Champney, J. 1993, Icarus, 106, 102

de la Fuente Marcos, C. & Barge, P. 2001, MNRAS, 323, 601

de la Fuente Marcos, C., Barge, P., & de la Fuente Marcos, R. 2002, J. Comp. Phys., 176, 276

Frank, J., King, A., & Raine, D. 1985, Accretion Power in Astrophysics (Cambridge: Cambridge University Press)

Gammie, C. 1996, ApJ, 457, 355

Gilman, P. & Glatzmaier, G. 1981, ApJS, 45, 335

Glatzmaier, G. & Gilman, P. 1981a, ApJS, 45, 351

—. 1981b, ApJS, 45, 381

Godon, P. & Livio, M. 1999, ApJ, 523, 350

—. 2000, ApJ, 537, 396

Goldreich, P. & Lynden-Bell, D. 1965, MNRAS, 130, 125

Goldreich, P. & Ward, W. 1973, ApJ, 183, 1051

Gottlieb, D. & Orszag, S. 1977, Numerical Analysis of Spectral Methods: Theory and Applications (Philadelphia: Society for Industrial and Applied Mathematics)

Gough, D. 1969, J. Atmos. Sci., 26, 448

Hawley, J. & Balbus, S. 1991, ApJ, 376, 223

Johansen, A., Andersen, A., & Brandenburg, A. 2004, A&A, 417, 361

Kida, S. 1981, J. Phys. Soc. Jpn., 50, 3517

Klahr, H. & Bodenheimer, P. 2003, ApJ, 582, 869

Klahr, H. & Henning, T. 1997, Icarus, 128, 213

Koller, J., Li, H., & Lin, D. 2003, ApJ, 596, L91

Kraichnan, R. 1967, Phys. Fluids, 10, 1417

Lesieur, M. 1997, Turbulence in Fluids (Dordrecht: Kluwer)

Li, H., Colgate, S., Wendroff, B., & Liska, R. 2001, ApJ, 551, 874

Li, H., Finn, J., Lovelace, R., & Colgate, S. 2000, ApJ, 533, 1023

Lin, D., Bodenheimer, P., & Richardson, D. 1996, Nature, 380, 606

Lovelace, R., Li, H., Colgate, S., & Nelson, A. 1999, ApJ, 513, 805

Marcus, P. 1986, in Proceedings of Astrophysical Radiation Hydrodynamics, ed. K.-H. Winkler & M. Norman (Springer-Verlag), 359–386

—. 1990, J. Fluid Mech., 215, 393

—. 1993, ARA&A, 31, 523

Marcus, P. & Press, W. 1977, J. Fluid Mech., 79, 525

Marcy, G. & Butler, R. 1998, ARA&A, 36, 57

Marcy, G., Cochran, W., & Mayor, M. 2000, in Protostars and Planets IV, ed. V. Mannings, A. Boss, & S. Russell (Tuscon: University of Arizona Press), 1285–1311

Mayor, M. & Queloz, D. 1995, Nature, 378, 355

Moore, D. & Saffman, P. 1971, in Aircraft Wake Turbulence and its Detection, ed. J. H. Olsen, A. Goldburg, & H. Rogers (New York: Plenum Press), 339–354

Ogura, Y. & Phillips, N. 1962, J. Atmos. Sci., 19, 73

Paret, J. & Tabeling, P. 1998, Phys. Fluids, 10, 3126

Pedlosky, J. 1979, Geophysical Fluid Dynamics (New York: Springer-Verlag)

Provenzale, A. 1999, Annu. Rev. Fluid Mech., 31, 55

Rogallo, R. 1981, Numerical experiments in homogeneous turbulence, Technical memorandum 81315, NASA

Safranov, V. 1960, Annales d'Astrophysique, 23, 979

Shakura, N. & Sunyaev, R. 1973, A&A, 24, 337

Shetty, S., Asay-Davis, X., Youssef, A., & Marcus, P. 2004, in preparation

Stone, J., Gammie, C., Balbus, S., & Hawley, J. 2000, in Protostars and Planets IV, ed. V. Mannings, A. Boss, & S. Russell (Tuscon: University of Arizona Press), 589–611

Tanga, P., Babiano, A., Dubrulle, B., & Provenzale, A. 1996, Icarus, 121, 158

Velikhov, E. 1959, Sov. Phys. – JETP, 36, 1398

Ward, W. 1997, Icarus, 126, 261

Weidenschilling, S. 1995, Icarus, 116, 433

Weidenschilling, S. & Cuzzi, J. 1993, in Protostars and Planets III, ed. E. Levy & J. Lunine (Tucson: University of Arizona Press), 1031–1060

Youssef, A. 2000, PhD thesis, University of California, Berkeley

This preprint was prepared with the AAS LaTeX macros v5.2.

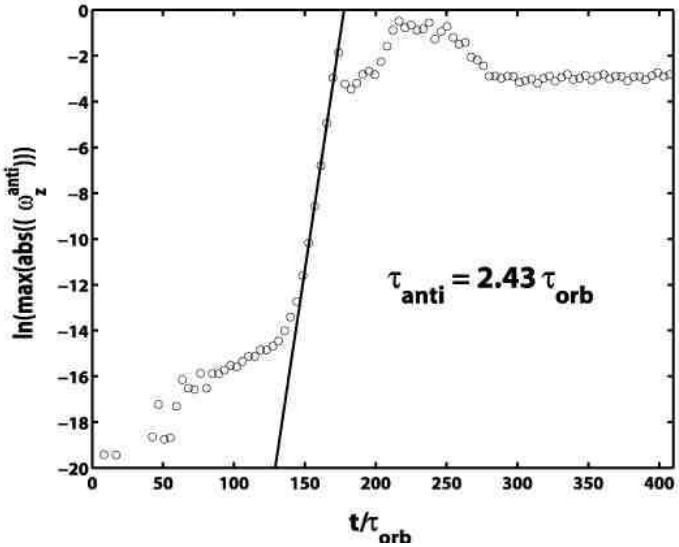

Fig. 9.— Growth of unstable antisymmetric linear eigenmode. Because the initial condition was symmetric with respect to the midplane, the instability could not be manifested until round-off error populated the antisymmetric modes. Eventually, the eigenmode emerges out of the noise, and grows exponentially fast, with an e-folding time of a few τ_{orb}.

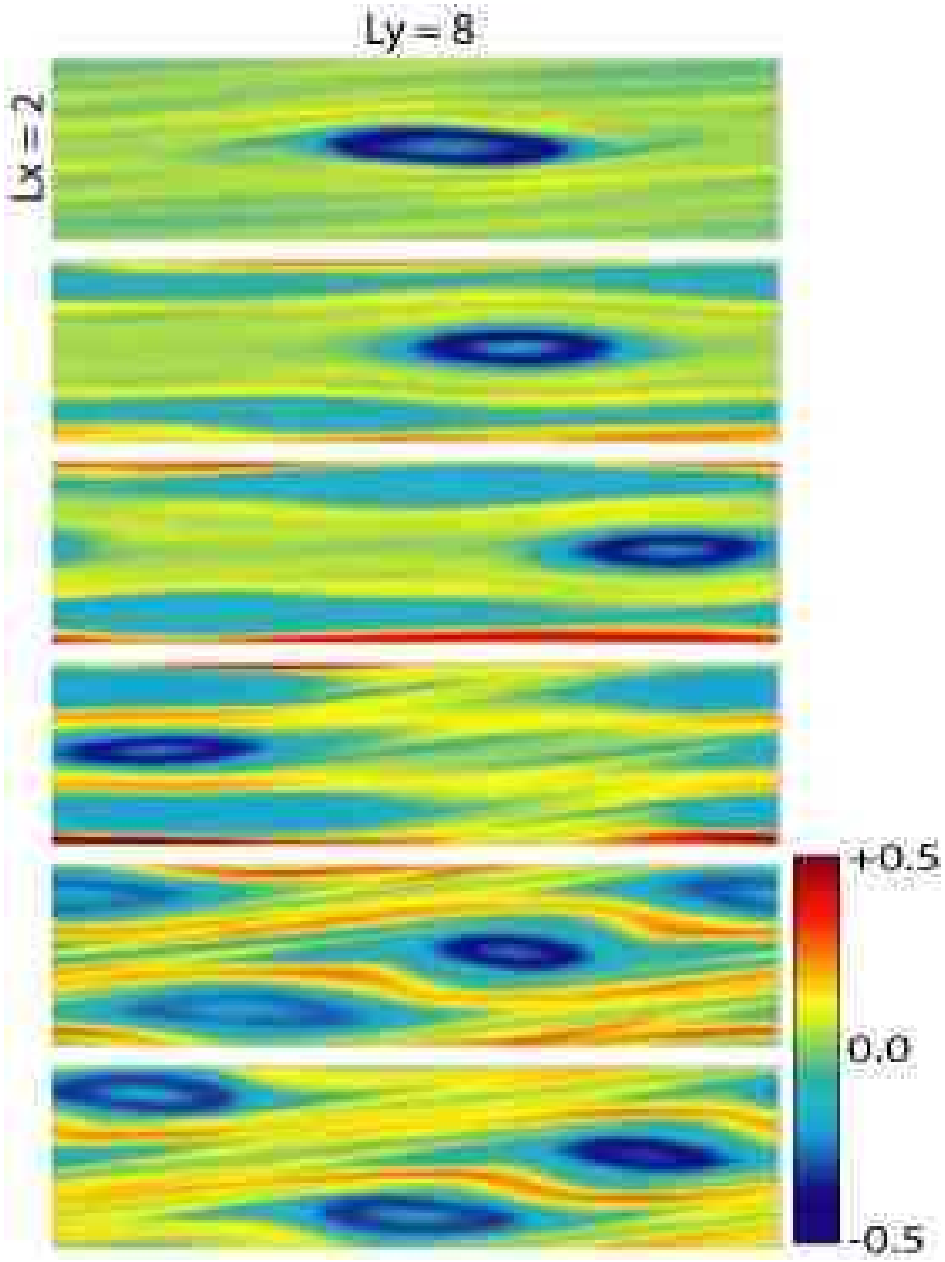

Fig. 10.— Simulation of an off-midplane vortex: $x-y$ slice at $z = 2$ of the z-component of vorticity $\tilde{\omega}_z$. Blue = anticyclonic vorticity, red = cyclonic vorticity. The time between frames is $\Delta t/\tau_{orb} = 42$. A single vortex from the last frame of Figure 6 was isolated and used as the initial condition for this run. Surprisingly, the other vortices reformed.

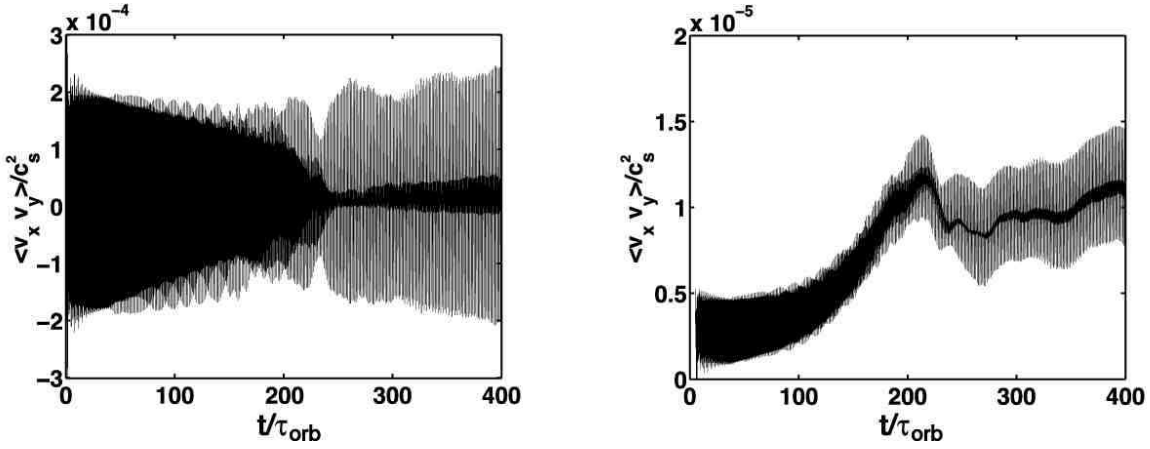

Fig. 11.— Velocity correlations as a function of time for the full simulation of a finite-height midplane vortex settling into a quasi-equilibrium, going unstable (at $t \approx 200\tau_{orb}$), then new, off-midplane vortices forming. The first panel shows the raw velocity correlations, whereas the second panel shows the same data smoothed with a window of $10\tau_{orb}$.